



“H” Shaped Echelon Joints Under Uniaxial Loading

Vahab Sarfarazi · Reza Khodakaram zadeh · Kaveh Asgari · Xiao Wang

Received: 10 July 2021 / Accepted: 5 September 2021 / Published online: 20 September 2021
© The Author(s), under exclusive licence to Springer Nature Switzerland AG 2021

Abstract In this investigation, the failure behaviour of “H” shaped non-persistent cracks under uniaxial load has been examined using experimental tests and Particle Flow Cod (PFC). Dimensions of produced concrete sample was $18\text{ cm} \times 18\text{ cm} \times 5\text{ cm}$. Inside the sample, one “H” shaped non-persistent joints were provided. The angles of the “H” shaped non-persistent joint were 0° , 30° , 60° , and 90° degrees. A total of 12 layouts were considered for pre-existing joints in which the larger joints were 60 cm long and the length of small crack was 2 cm. the opening of crack was 1 mm. Also, the 24 specimens with different non-persistent joints were numerically modeled. Rate of applied axial load to the model was 0.05 mm/min. Tensile strength of concrete was 1 MPa. Model was calibrated by try and error. The outcomes indicate that the crack propagation was mainly controlled by both the angle of the non-persistent joint relative to the loading direction and joint length. The compressive

strength of the samples varied with the layout and failure mode of the joints. It was shown that the failure behavior of discontinuities was referred to the number of the induced tensile cracks which were augmented by augmenting the joint angle. The strength of specimens increased by decreasing the angle of joint and joint length. The strength and failure process were similar in both approaches i.e., the laboratory tests and the numerical modeling.

Keywords PFC2D · Physical test · “H” shape non-persistent joint · Joint angle

1 Introduction

One of the natural geological substances is rock mass. This material usually includes intact rock and discontinuities at diverse scales, like fracture, joints, weak bedding and faults (Einstein 1983). There are some parameters which affect the stability of rock mass engineering, such as characteristics of intact rock and, in higher degree, discontinuities within the rock mass (Bobet 2000). Non persistent joints are indicated as a discontinues set of joints. These kinds of joints usually are observed in the engineering surrounding rock mass, like sliding slope (Brideau 2009; Siad 1998; Huang 2015), mine pillar in the underground (Lajtai 1994; Esterhuizen 2011), etc. According to rock engineering accidents, most of instability failure in

V. Sarfarazi (✉) · R. K. zadeh
Department of Mining Engineering, Hamedan University
of Technology, Hamedan, Iran
e-mail: sarfarazi@hut.ac.ir

K. Asgari
Department of Mining Engineering, Shahid Bahonar
University of Kerman, Kerman, Iran

X. Wang
School of Civil Engineering, Southeast University,
Nanjing 210089, China

rock engineering is due to the fact that under environmental stress (such as blasting, initial in-situ stress, earthquake and excavation unloading), internal discontinuities propagate and coalesce with each other (Zang 2020; Wang 2019; Zhang 2019). Thus, for evaluating and maintaining the stability of rock engineering, a complete comprehend of the fracturing behavior in surrounding rock is needed. Although, due to the hard condition of insitu studying of crack coalescence behavior, most of investigations have been done on rock-like or real rock samples with pre-fabricated discontinuities, and some interesting outcomes have been found. Experiments have shown that under compression loading, two kinds of new cracks happen at or adjacent to the joint tip which included: wing cracks and secondary cracks (Lajtai 1974). The first crack producing by tension was wing crack, which it is begun at or adjacent to the prefabricated joint tip and spreads across the maximum principal stress. Initiation of secondary crack was from edges of the prefabricated joint and it is divided into secondary coplanar cracks and secondary oblique cracks. In the case of sample contains more than one joints, besides, the initiation and spread of the cracks, there is also coalescence of cracks which is also the focus of investigation of behavior of cracks. In recent years, several loading experiments have been performed to examine the mechanical characteristics and cracking process of samples with few joints, including two joints (Lee 2011; Wong 2009), three joints (Park 2010; Wong 2001), and four joints (Zhou 2014; Yang 2017). Non-persistent joints, usually occurs in sets and they are often arranged with specific inclinations. These joints are generally found in rock engineering of surrounding rock. In the process of loading, the presence of several cracks leads to the super imposition of stress fields around joints besides, it has some effects on mode of crack coalescence between joints. Thus, in the case of presence of multiple joints, mode of the crack coalescence is more complex in comparison with a case with less joints (Bahaaddini 2013; Wang 2019; Sun 2019; Wu 2020; Song 2020; Sun 2020; Jiang 2020; Wang 2019). To comprehend the effect of joint arrangement on mechanical characteristics and failure modes of samples, several experimental investigations have been performed (Sagong 2002; Prudencio 2007; Yang 2019). In addition to studies related to mechanical parameters and failure modes, some scientists have examined in a micro

approach and more specifically, moreover they have investigated the performance of news technologies which have made a research on the micro-fracture process possible. The new technologies such as, microscopic observation (Cheng 2018), computed tomography (CT) scanning (DeSilva 2018; Zhang 2019; Zhou 2008), the acoustic emission (AE) technique (Naderloo 2019; Lei 2004; Chen 2019; Zhang 2020) and digital image correlation (DIC) (Li 2017; Chen 2019; Wu 2020). Various numerical approaches such as including FLAC (Fu 2016), UDEC (Farahmand 2018), PFC (Huang 2019), RFPA (Wang 2014), DDA (Shi 1992), ELFEN (Pine 2007), PD (Wang 2018), etc. Particle Flow Code (PFC) based on the Discrete Element Method (DEM) has been performed to study the mechanical behavior and fracturing process of samples containing joints for modelling the failure process of jointed rocks. The principal advantage of PFC compared to other simulations programs is that it doesn't need complicated fracture criteria (Zhang 2012). Several investigations have indicated that PFC is a suitable approach for modeling the problems of cracking in rock (Zhang 2012; DeSilva 2018; Yang 2019; Yang 2015). Investigation of cracking process of rock-like samples containing one and two pre-existing joints using PFC was performed by Zhang and Wong, 2012. In this study, uniaxial compression experiments on samples containing "H"- shaped non-persistent joints in the laboratory were followed by numerical simulations with PFC2D. Two parameters of joint direction with respect to the loading axis and shape of joints were varied in the test programs, and the evolutions of the failure pattern and compressive strength were investigated.

2 Uniaxial Compression Testing of Specimens with H Shaped Joints

Tables 1, 2, 3 summarizes the mixture design and specifications of different ingredients used to prepare the concrete specimens.

The specimens had a length of 18 cm, a width of 18 cm, and a height of 5 cm (Fig. 1). In order to create the cracks, 1 mm thick metal sheets were first placed in the mold and were then pulled upward after the initial setting of the concrete.

Table 1 Mixture design used in this study

Gravel (gr)	Sand (gr)	Cement (gr)	Water (cc)	Superplasticizer (gr)	Micro silica (gr)
3000	10,500	2800	1500	120	90

Table 2 characteristics of cement and Silica fume

Properties	Cement	Silica fume
Physical properties		
Specific gravity (gr/cm ³)	3.15	2.2
Surface area (m ² /kg)	320	20,000
Size (micron)	–	0.1
Bulk density (kg/m)	–	576
Initial setting time (min)	45	–
Final setting time (min)	375	–
Chemical properties (percentage)		
SiO ₂	90–96	20–25
Al ₂ O ₃	0.5–0.8	4–8

Table 3 Physical properties of sand

Index	Value
Specific gravity (gr/cm ³)	2.63
Passing 4.75-mm sieve (%)	100
Maximum dry density (kN/m ³)	15.5
Minimum dry density (kN/m ³)	12.3
D ₁₀	0.194
D ₅₀	0.322
D ₆₀	0.344

The length of large joints and small joints was 6 cm and 2 cm, respectively. The dip angle of the middle small joint was 0°, 30°, 60°, and 90° degrees, and the large joints were perpendicular to the small joint (Figs. 2, 3, 4 and 5). Distance between the joints were 2 cm, 2.75 cm and 3.5 cm. The samples were preserved in a cool and ventilated room for 28 days. A total of 12 layouts were considered for pre-existing joints. To minimize the random error and augment the reliability of the results, three identical samples were created and tested for each layout.

The compression load was applied to the specimens in the vertical direction using servo-controlled apparatus with a deformation rate of 0.05 mm/min (Fig. 6).

2.1 The Failure Process Observed Experimentally

2.1.1 Angle of Middle Joint was 0°

Figure 7 a–c indicates samples failure pattern including three non—persistent joints with middle joint angle of 0°. When distance between the joints was 2 cm, 2.75 and 3.5 cm (Fig. 7 a, b and c), two tensile cracks engendered from middle joint wall and circulated parallel to loading axis until intermingle with model boundary.

2.1.2 Angle of Middle Joint was 30°

Figure 8 a–c indicates samples failure pattern including three non—persistent joints with middle joint angle of 30°. When distance between the joints was 2 cm, 2.75 cm and 3 cm (Fig. 8 a, b and c), two tensile cracks originate from tips of larger joints and circulated parallel to loading axis until integrate with model boundary.

2.1.3 Angle of Middle Joint was 60°

Figure 9 a–c indicates samples failure pattern including three non—persistent joints with middle joint angle of 60°. When distance between the joints was 2 cm, 2.75 cm and 3 cm (Fig. 9 a, b and c), four tensile cracks originated from middle joint tips and circulated parallel to loading axis until intermingle with tips of larger joints. Furthermore, two tensile cracks originate from tips of larger joints and circulated parallel to loading axis until integrate with model boundary.

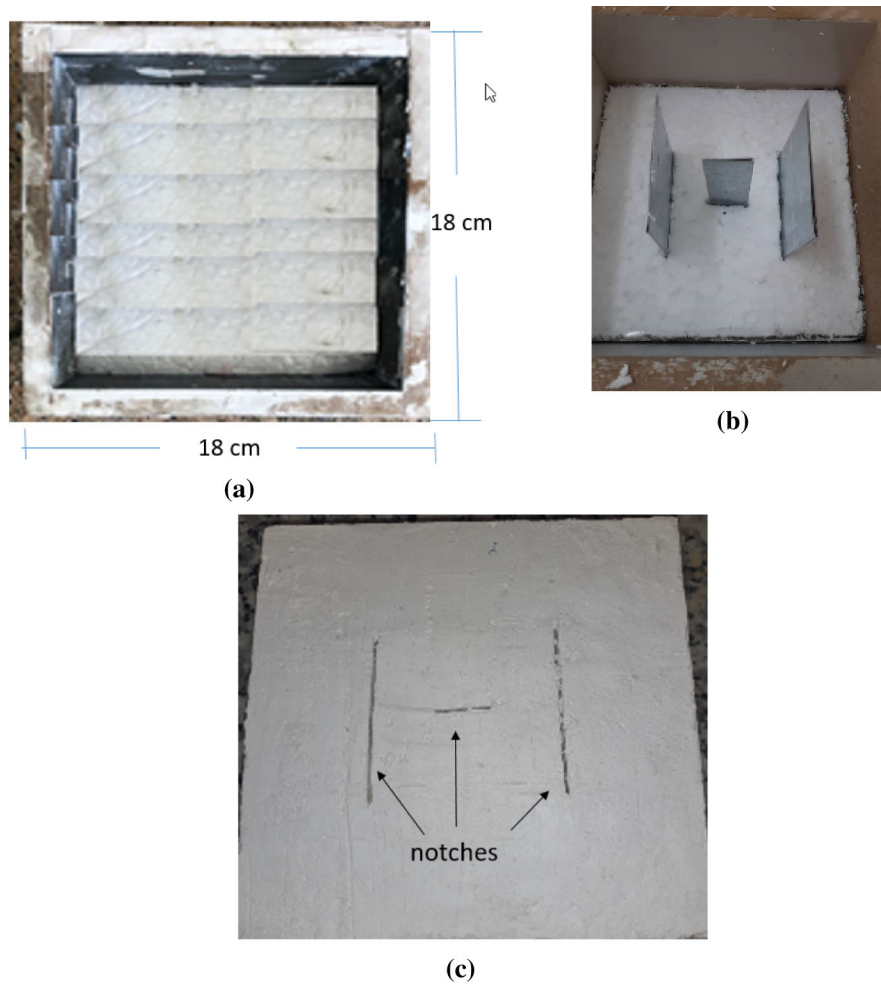


Fig. 1 (a) Frame with dimensions of 18 cm * 18 cm * 5 cm, (b) mold containing three steel sheets, (c) the specimen after removing the sheets

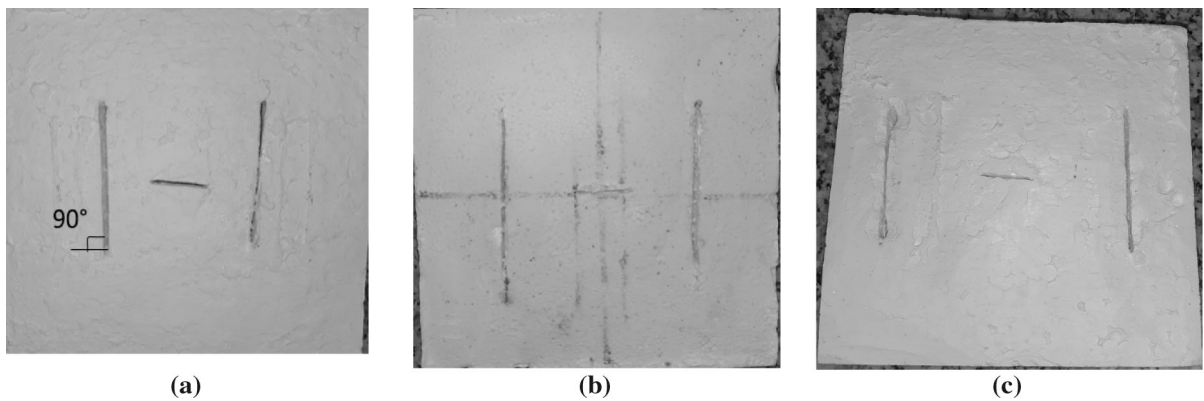


Fig. 2 Distance between the H shaped joints were a 2 cm, b 2.75 cm and c 3.5 cm; middle joint angle of 0°

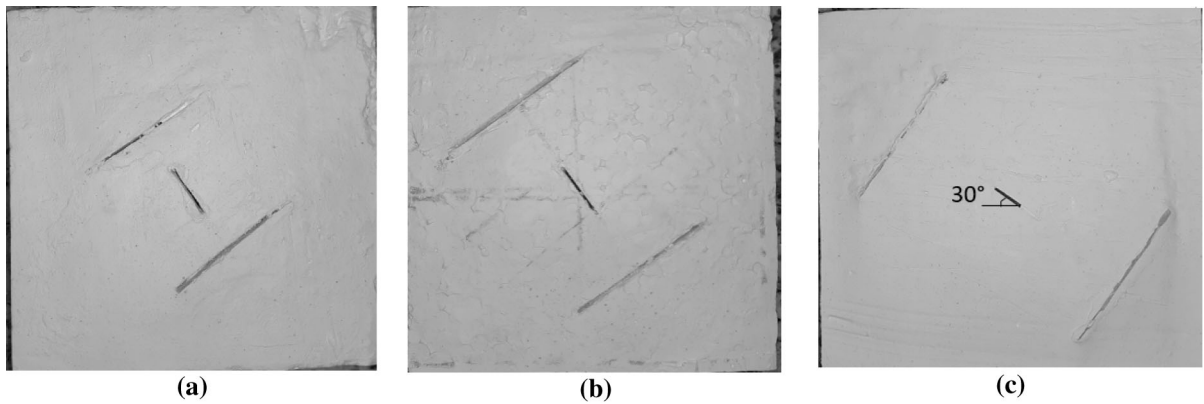


Fig. 3 Distance between the H shaped joints were **a** 2 cm, **b** 2.75 cm and **c** 3.5 cm; middle joint angle of 30°

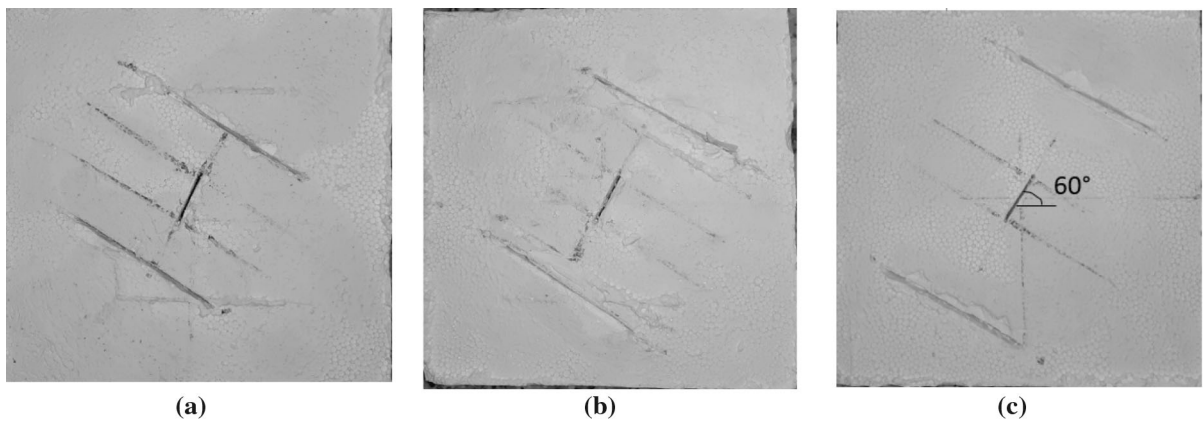


Fig. 4 Distance between the H shaped joints were **a** 2 cm, **b** 2.75 cm and **c** 3.5 cm; middle joint angle of 60°

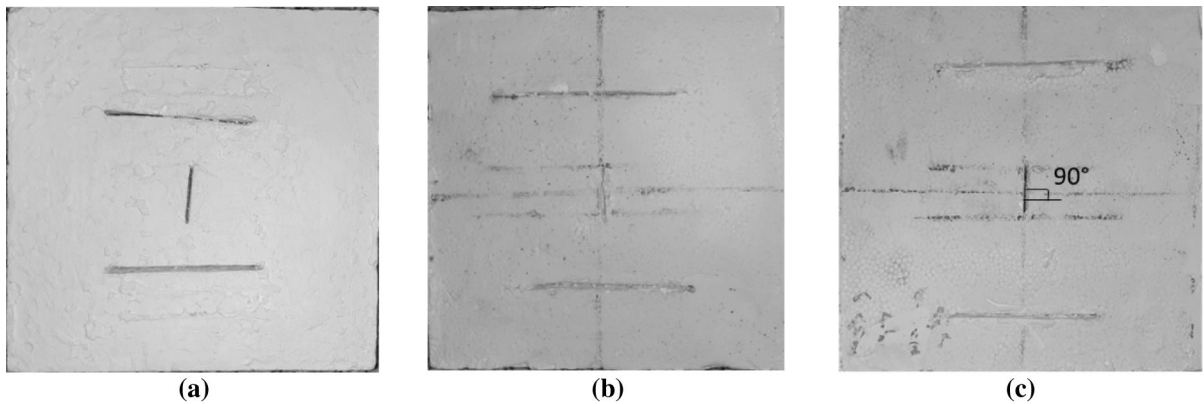


Fig. 5 Distance between the H shaped joints were **a** 2 cm, **b** 2.75 cm and **c** 3.5 cm; middle joint angle of 90°

2.1.4 Angle of Middle Joint was 90°

Figure 10 a-c indicates samples failure pattern including three non—persistent joints with middle joint

angle of 90°. When distance between the joints was 2 cm, 2.75 cm and 3 cm (Fig. 10 a, b and c), one tensile crack originated between two horizontal joints and circulated parallel to loading axis until intermingle



Fig. 6 Specimen placed between the plates of the loading machine

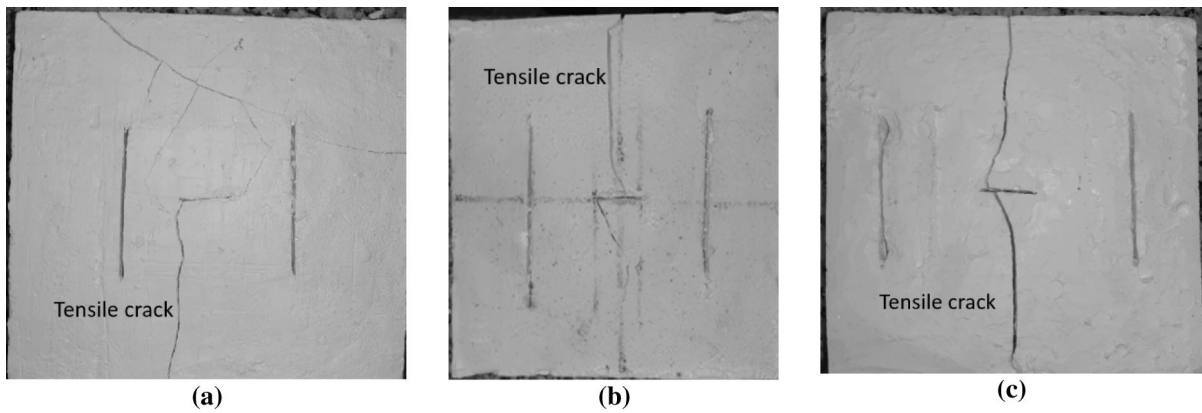


Fig. 7 Failure pattern of sample containing the H shaped joints with joint spacing of **a** 2 cm, **b** 2.75 cm, **c** 3.5 m; middle joint angle of 0°

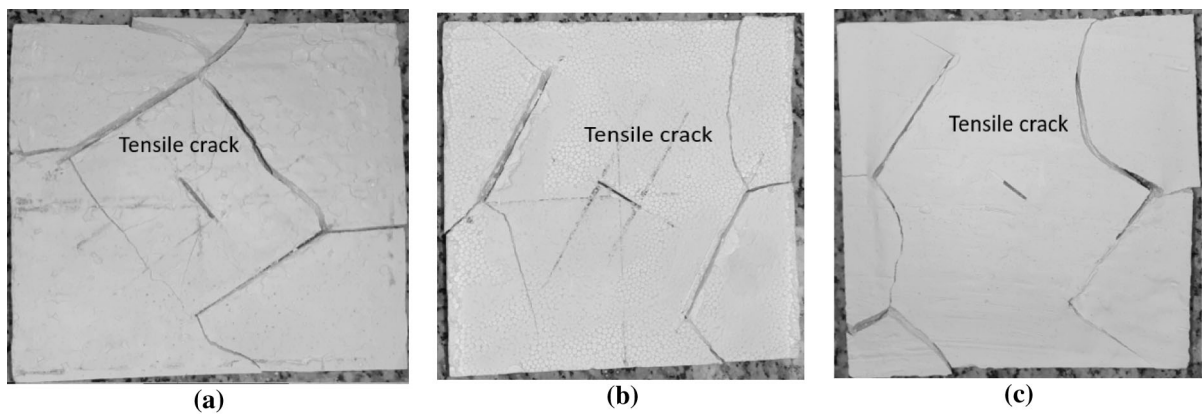


Fig. 8 Failure pattern of sample containing the H shaped joints with joint spacing of **a** 2 cm, **b** 2.75 cm, **c** 3.5 m; middle joint angle of 30°

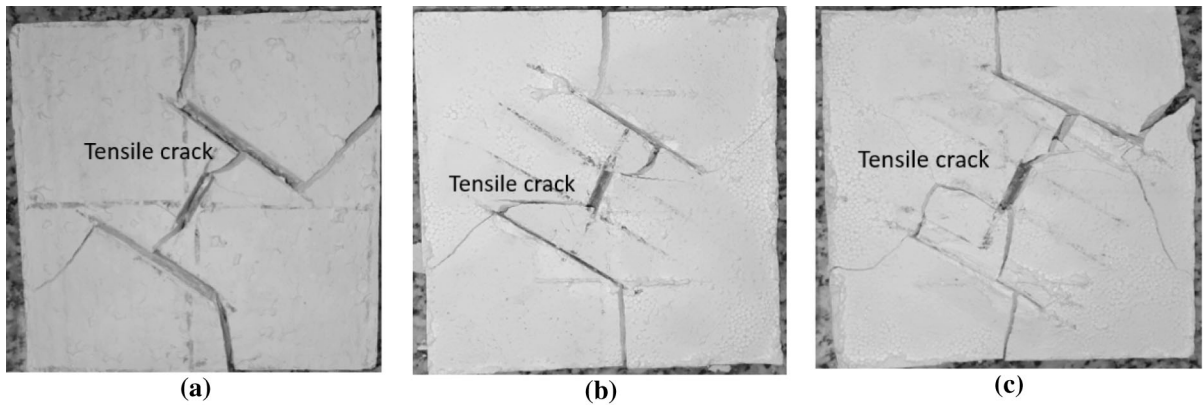


Fig. 9 Failure pattern of sample containing the H shaped joints with joint spacing of **a** 2 cm, **b** 2.75 cm, **c** 3.5 m; middle joint angle of 60°

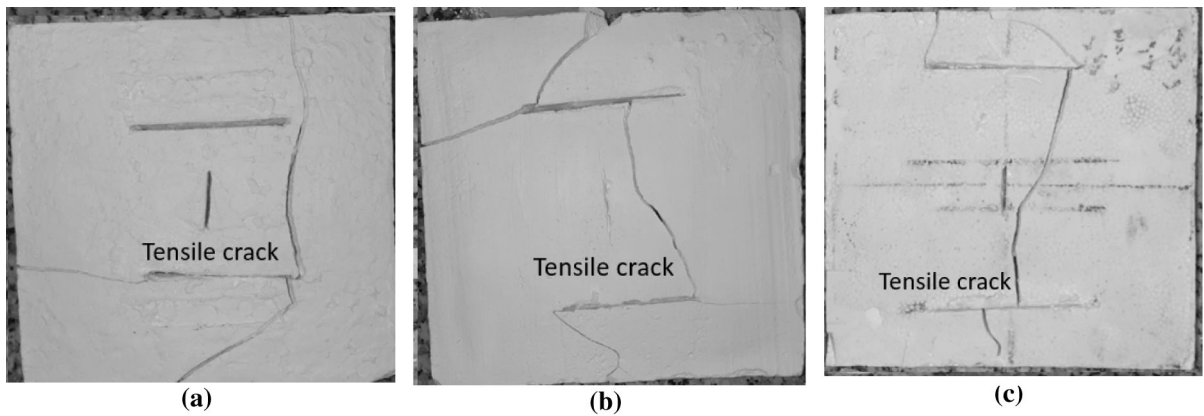


Fig. 10 Failure pattern of sample containing the H shaped joints with joint spacing of **a** 2 cm, **b** 2.75 cm, **c** 3.5 m; middle joint angle of 90°

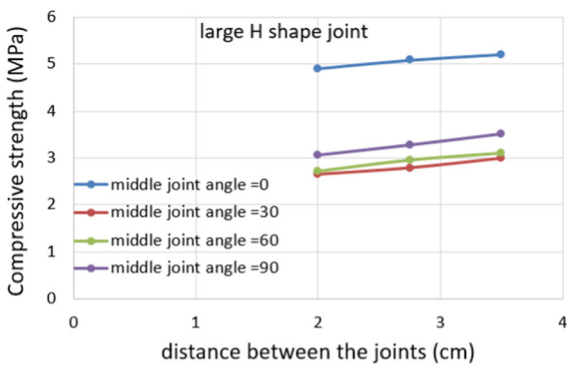


Fig. 11 Effects of distance between the joints on the specimens' strength for four different cases of middle joint angle

with walls of larger joints. Furthermore, two tensile crack originate from walls larger joints and circulated parallel to loading axis until integrate with model boundary.

2.2 The Influence Joint Angles on the Specimens' Strength

Figure 11 represents the effects of distance between the joints on the specimens' strength for four different cases of middle joint angle. The minimum and maximum strengths of samples occurred when joint angle were 30° and 0°, respectively. The strength of samples decrease by decreasing the distance between the joints. In this condition the stress concentration at

the joints' tips increase by decreasing the distance between the joints. This leads to decreasing the compressive strength.

3 Numerical Analysis of the Specimens

3.1 Specimens' Modeling by PFC2D

Potyondy 2012, presented the flat-joint (FJ) model taking into account the particles' polygonal grain structure [45–48]. The local FJ contact is considered as the flat notional surfaces centered at the contact points, which is rigidly closed to an individual particle. Each part's notional surface is called face and interacting with other neighboring particles at the contacting piece's face. Hence, each faced particle (grain) is represented as a spherical (in 3D) or circular (in 2D) core with the skirted faces. Therefore, such faces are considered as disks (in 3D) or lines (in 2D). The particles bonded assembly by FJ contacts is known as flat-jointed materials (FJM). Each element can be un-bonded or bonded by discretizing the interface within faced grains into the elements. After installing FJ for each grain–grain contact, the moment and force at each element are kept as zero and they are updated in terms of the relative motion of faces and force–displacement law of bond. In a direct mode, the normal force is updated first and the shear force is updated within an incremental mode. The bonded element's behavior is still linear elastic until exceeding the strength limit. The maximum and shear stresses normal of elements ($\sigma_{max}^{(e)}, \tau_{max}^{(e)}$) are determined as,

$$\sigma_{max}^{(e)} = \frac{-\bar{F}_{(e)}^n}{A^{(e)}} \quad (1)$$

$$\tau_{max}^{(e)} = \frac{\bar{F}_{(e)}^s}{A^{(e)}} \quad (2)$$

where $A^{(e)}$ represents the element area and $\bar{F}_{(e)}^n$ and $\bar{F}_{(e)}^s$ denote respectively shear and normal forces performing on the elements. The elements' rotational resistance is presented by faced grains' special structure and the moment contributions are insignificant. It was indicated that the FJ elements can be un-bonded or bonded. The bonded element's strength is computed by the Coulomb criterion with the tension cut-off. If the induced normal stress is higher than the element

tensile strength ($\sigma_{max}^{(e)} > \sigma_b$), the element breaks in tension after the generation of the tensile crack and modifying the element to the un-bonded state. The element's shear strength is stated by the bond cohesion c_b and the local friction angle ϑ_b . When the induced shear stress gets higher than the shear strength of element [$\tau_{max}^{(e)} > \tau_c = c_b - \bar{\sigma} \tan \vartheta_b$], the bond breaks in shear while modifying the bond state to un-bonded with residual frictional strength. Moreover, the un-bonded element has linear elastic mechanical behavior with frictional slip. However, based on the Coulomb criterion with the tension cut-off, the force–displacement law can be expressed as follows,

$$\bar{\sigma} = \begin{cases} 0 & \bar{g} \geq 0 \\ -k_n \bar{g} & \bar{g} < 0 \end{cases} \quad (3)$$

$$\bar{\tau} = \begin{cases} -\bar{\sigma} \tan \vartheta_r & \bar{\sigma} < 0 \\ 0 & \bar{\sigma} = 0 \end{cases} \quad (4)$$

where \bar{g} represents the gap of element, $\tan \vartheta_r$ is the friction coefficient of the un-bonded element, ϑ_r shows the residual friction angle. Breaking each bonded element leads to a partial damage of the FJ contact. By the relative displacement at a FJ contact higher than the FJ diameter, the faces are removed. Moreover, re-contacting such particles, the force–displacement association is that of the linear contact model. Limitations of DEM should be mentioned as: (a) Fracture is closely related to the size of elements, and that is so called size effect. (b) Cross effect exists because of the difference between the size and shape of elements with real grains. (c) In order to establish the relationship between the local and macroscopic constitutive laws, data obtained from classical geomechanical tests which may be impractical are used (Potyondy 2012, 2015, 2017; Potyondy 2004; Ghazvinian 2012).

3.2 Preparing and Calibrating the PFC2D Model for Rock-Like Material

The Brazilian tensile strength test was used to calibrate the PFC2D software for performing the simulation of both of the gypsum and grout materials (gypsum as base model and grout as joint filling). This computer code can model the testing specimens through a standard process of generating a particle assembly by

Table 4 Micro features utilized to characterize the grout

Particle micro properties		Flat-joint micro properties	
Model height (mm)	108	Gap ratio	0.5
Model width (mm)	54	Ec (GPa)	0.3
Kn/ks	1.7	Bonded friction	0.83
Density (kg/m ³)	2800	Tensile strength (MPa)	0.1
Minimum particle diameter (mm)	0.54	Tensile strength standard deviation (MPa)	0.01
Maximum particle diameter (mm)	1.08	Cohesion (MPa)	0.5
Ec(GPa)	0.3	Cohesion standard deviation (MPa)	0.05
Porosity	0.08	Number of elements	2
		Kn/ks	1.7

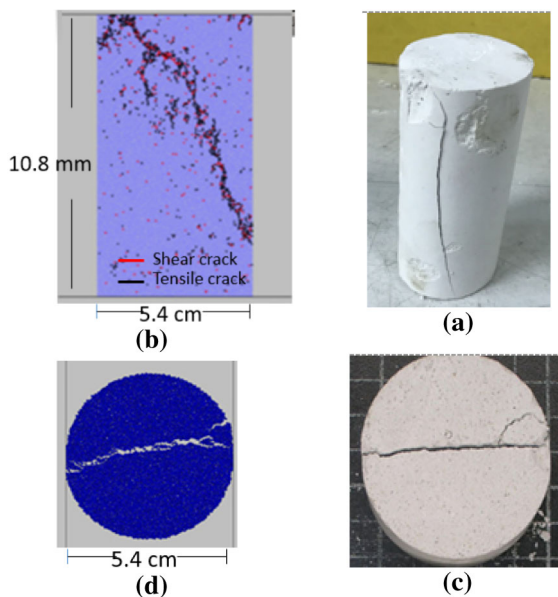


Fig. 12 (a) Laboratory compression experiment, (b) Simulated compression experiment, (c) Laboratory Brazilian experiment and (d) Simulated Brazilian experiment

the following four steps: (1) particle generating and packing of the model, (2) installing an isotropic stress condition, (3) the elimination of the floating particles from the model and (4) installing the particle bonds in the model assembly (Ghazvinian 2012). Therefore, by considering the calibrated micro-properties given in Table 4, calibrated particle assemblies were created

Table 5 Comparison between macro-mechanical properties obtained by experiments and modelling

Mechanical properties	Experimental results	PFC2D Model results
Elastic modulus, (GPa)	4.67	4.7
Poisson’s ratio	0.18	0.19
UCS, (MPa)	8	8.4
Brazilian tensile strength (MPa)	1	1.2

for modeling the grout specimens in PFC2D. Damping factor was equal to 0.7 according to PFC manual. The porosity value was equal to 0.08. Figures 12a and b indicate the laboratory uniaxial compression test and its numerical simulation, respectively. Figures 12c and d show the experimental Brazilian test and its numerical simulation, respectively. The results indicate well match between the experimental test and numerical simulation. In addition, the values of the macro-parameters obtained by numerical modeling namely young’s modulus, Poisson’s ratio, and UCS values are in good accordance with the experimentally measured values (Table 5).

3.3 Numerical Simulation of the Specimens with H Shape Joints

Numerical simulation uniaxial tests for jointed rock were performed by creating cubic model in the PFC2D (by using the calibrated micro-parameters) (Figs. 13, 14, 15, 16, 17, 18, 19 and 20), after calibration of PFC2D. The PFC sample had the dimension of 18 cm * 18 cm. The circle sample were made by a total of 15,342 disks with a minimum radius of 0.027 cm. Two walls locate at the top and bottom of the model. By eliminating bands of particles from model, non-persistent H joints were created (Figs. 13, 14, 15, 16, 17, 18, 19 and 20).

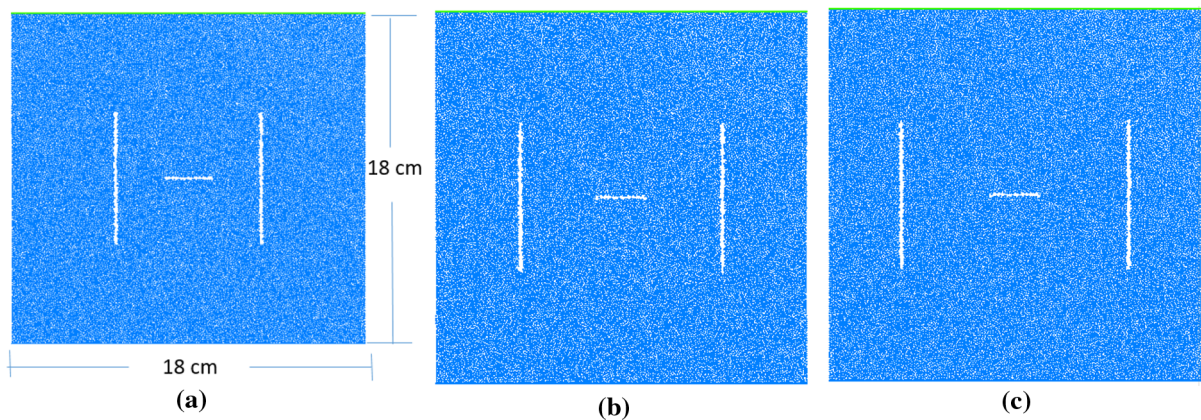


Fig. 13 Distance between the large H shaped joints were **a** 2 cm, **b** 2.75 cm and **c** 3.5 cm; middle joint angle of 0°

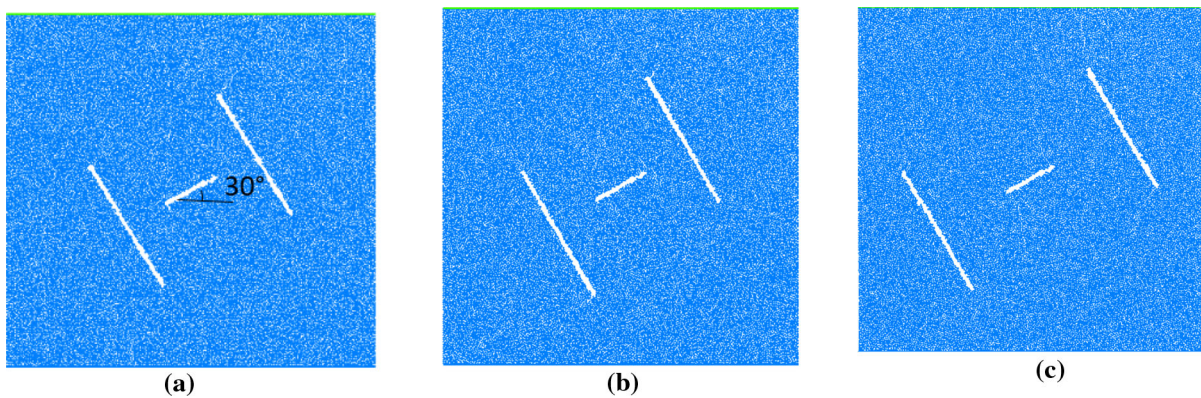


Fig. 14 Distance between the large H shaped joints were **a** 2 cm, **b** 2.75 cm and **c** 3.5 cm; middle joint angle of 30°

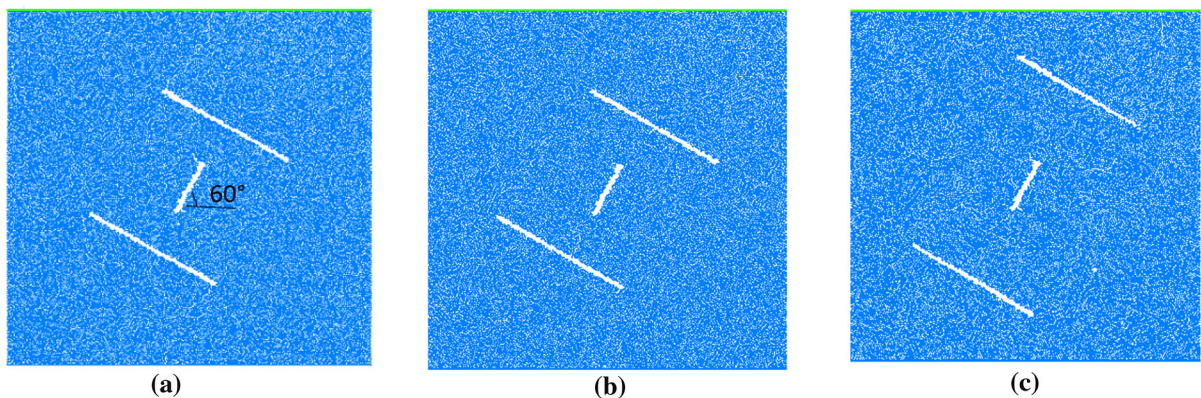


Fig. 15 Distance between the large H shaped joints were **a** 2 cm, **b** 2.75 cm and **c** 3.5 cm; middle joint angle of 60°

Generally, the models including three non-persistent H shape joints were formed. Two type of H shape joints were built i.e., large H shape joints (Figs. 13–

16) and small H shape joints (Figs. 17–20). In large H shape joints, the lengths of two parallel joints were 6 cm and the length of middle joint was 2 cm

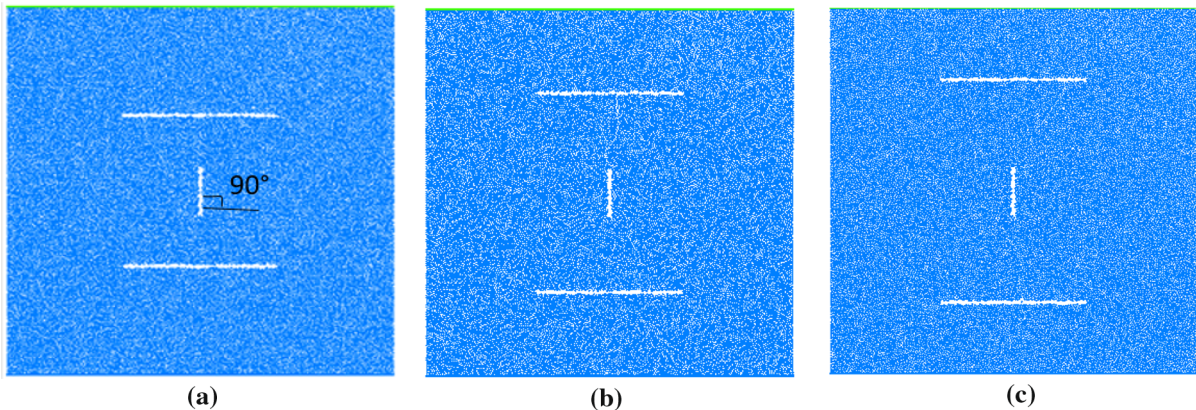


Fig. 16 Distance between the large H shaped joints were **a** 2 cm, **b** 2.75 cm and **c** 3.5 cm; middle joint angle of 90°

(Figs. 13–16). In small H shape joints, the lengths of two parallel joints were 2 cm and the length of middle joint was 6 cm (Figs. 17–20). The angle of middle joints was change between 0° and 90° by increments of 30° (Figs. 13–20). In each joint angle, distance between the joints were 2 cm, 2.75 cm and 3.5 cm (Figs. 13–20 a, b and c). The configuration of large H shape joints was similar to experimental one. 24 different models have been built to investigate the impact of joint angle and joint configurations on the failure mechanism. The prefabricated cracks were 1 mm wide. Top and bottom walls was induced uniaxial force on the model. The value of loading rate in numerical simulation as 0.05 mm/min. The compression force was registered by registering the reaction forces on the top wall.

3.4 The Modelled Bond Forces Before the Crack Initiation Process

3.4.1 Large H Shape Joints

The distribution of bond force (as indicated in Figs. 21, 22, 23 and 24) showed the state of force vectors inside the modelled specimens prior to initiation of crack. The red and black lines indicated in Figs. 21, 22, 23 and 24 represent of the vectors of tensile and compression force in the model, respectively. The thick lines and their accumulation show the spaces where bigger forces are applied on the model. It is shown that at the tip of the crack, there are more compressive force, compared to the tensile forces of the bonded particles, thus, the initiation of tensile crack is the dominant mode of fracturing that

originates at the tip of the crack within the modelled specimens. It's worthy to note that the tensile force was concentrated around larger joints. It means that the tensile cracks were originated at these locations.

3.4.2 Small H Shape Joints

The distribution of bond force (as indicated in Figs. 25, 26, 27, 28) showed the state of force vectors inside the modelled specimens prior to initiation of crack. The red and black lines indicated in Figs. 25–28 represent of the vectors of tensile and compression force in the model, respectively. The thick lines and their accumulation show the spaces where bigger forces are applied on the model. It is shown that at the tip of the crack, there are more compressive force, compared to the tensile forces of the bonded particles, thus, the initiation of tensile crack is the dominant mode of fracturing that originates at the tip of the crack within the modelled specimens. It's worthy to note that the tensile force was concentrated around larger joints. It means that the tensile cracks were originated at these locations.

3.5 The Effects of H Shape Joint Configuration on the Failure Behavior of the Modelled Samples

3.5.1 Large H Shape Joints

3.5.1.1 Angle of Middle Joint was 0° Figure 29 a-c indicates samples failure pattern including three non—persistent joints with middle joint angle of 0° . Red line and black line indicated shear crack and

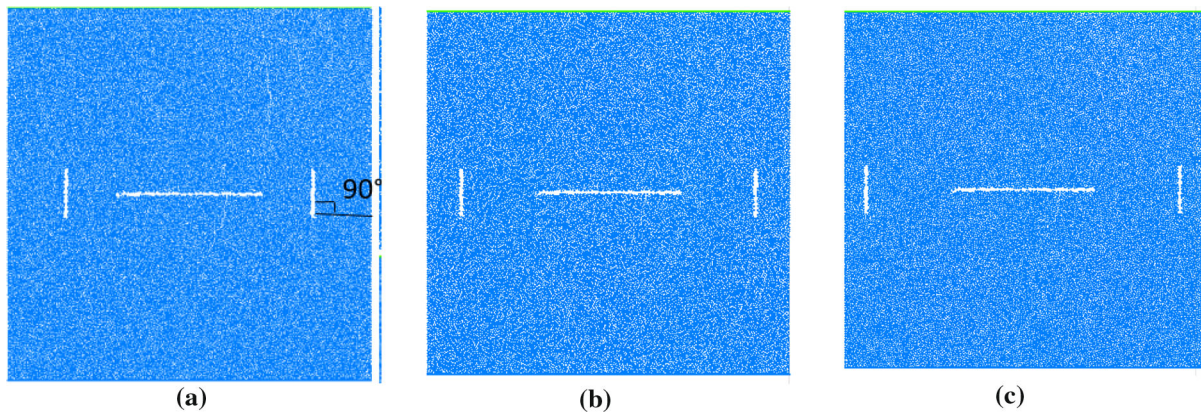


Fig. 17 Distance between the small H shaped joints were **a** 2 cm, **b** 2.75 cm and **c** 3.5 cm; middle joint angle of 0°

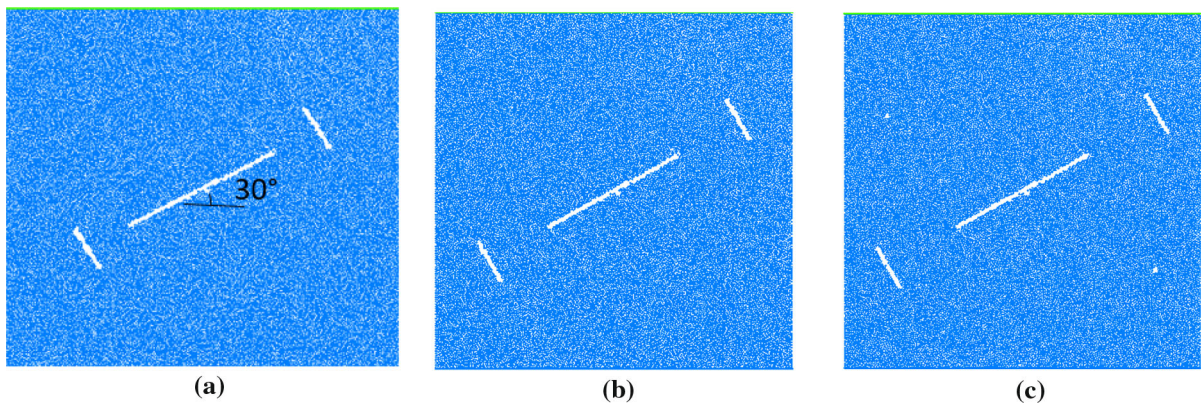


Fig. 18 Distance between the small H shaped joints were **a** 2 cm, **b** 2.75 cm and **c** 3.5 cm; middle joint angle of 30°

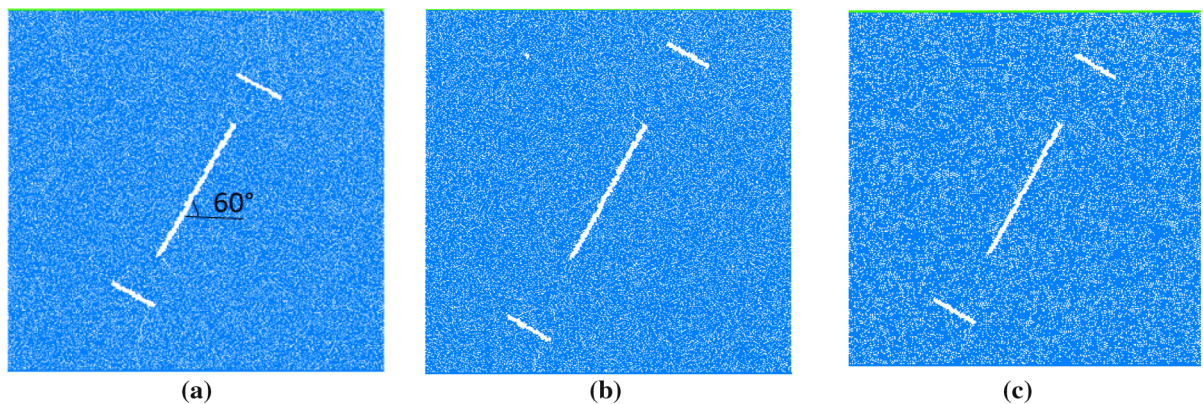


Fig. 19 Distance between the small H shaped joints were **a** 2 cm, **b** 2.75 cm and **c** 3.5 cm; middle joint angle of 60°

tensile crack, respectively. When distance between the joints was 2 cm, 2.75 cm and 3.5 cm (Fig. 29a, b and c), two tensile cracks engendered from middle joint tips and circulated parallel to loading axis until

intermingle with model boundary. Furthermore, two tensile cracks originate from middle joint wall and circulated parallel to loading axis.

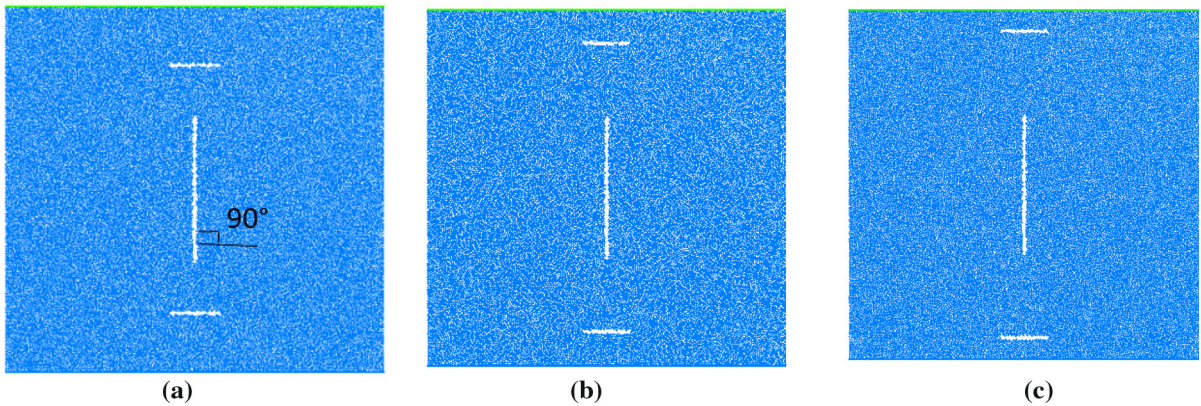


Fig. 20 Distance between the small H shaped joints were **a** 2 cm, **b** 2.75 cm and **c** 3.5 cm; middle joint angle of 90°

3.5.1.2 Angle of Middle Joint was 30° Figure 30 a-c indicates samples failure pattern including three non—persistent joints with middle joint angle of 30°. Red line and black line represented shear crack and tensile crack, respectively. When distance between the joints was 2 cm, 2.75 cm and 3 cm (Fig. 30a, b and c), two tensile cracks engendered from middle joint tips and circulated parallel to loading axis until intermingle with tips of larger joints. Furthermore, two tensile cracks originate from tips of larger joints and circulated parallel to loading axis until integrate with model boundary.

3.5.1.3 Angle of Middle Joint was 60° Figure 31 a-c indicates samples failure pattern including three non—persistent joints with middle joint angle of 60°. Red line and black line represented shear crack and tensile crack, respectively. When distance between the

joints was 2 cm, 2.75 cm and 3 cm (Fig. 31a, b and c), four tensile cracks originated from middle joint tips and circulated parallel to loading axis until intermingle with tips of larger joints. Furthermore, two tensile cracks originate from tips of larger joints and circulated parallel to loading axis until integrate with model boundary.

3.5.1.4 Angle of Middle Joint was 90° Figure 32 a-c indicates samples failure pattern including three non—persistent joints with middle joint angle of 90°. Red line and black line represented shear crack and tensile crack, respectively. When distance between the joints was 2 cm, 2.75 cm and 3 cm (Fig. 32 a, b and c), two tensile cracks originated from middle joint tips and circulated parallel to loading axis until intermingle with walls of larger joints. Furthermore, two tensile cracks originate from walls

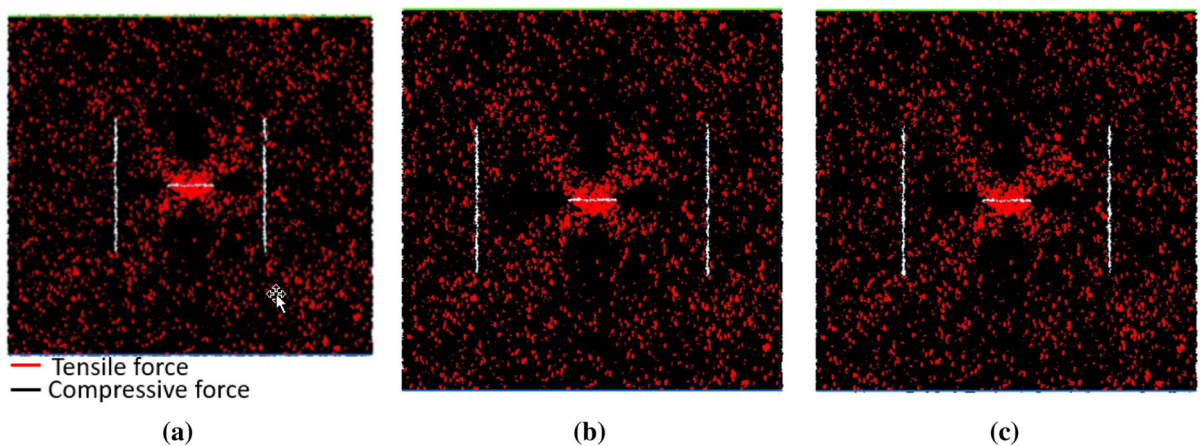


Fig. 21 Bond force distribution in models with joint spacing of **a** 2 cm, **b** 2.75 cm and **c** 3.5 cm; middle joint angle of 0°

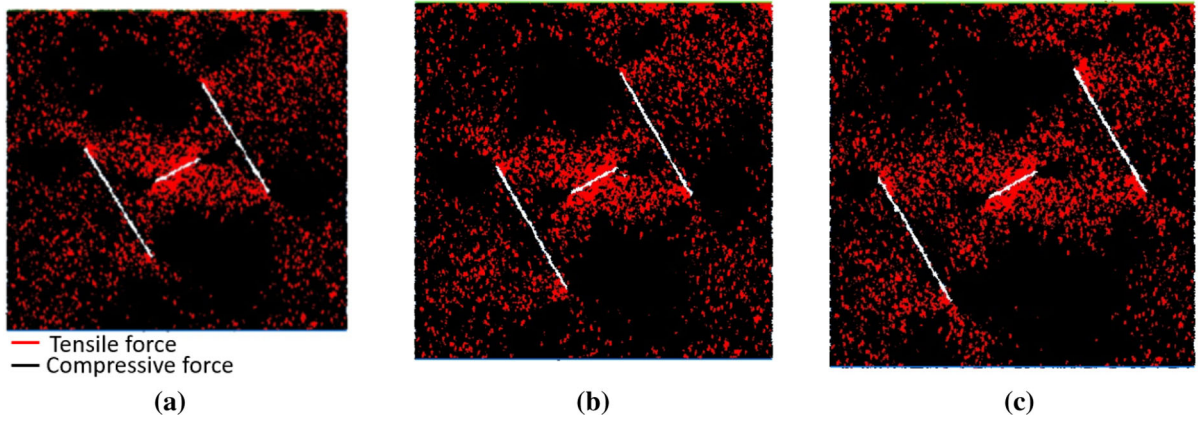


Fig. 22 Bond force distribution in models with joint spacing of **a** 2 cm, **b** 2.75 cm and **c** 3.5 cm; middle joint angle of 30°

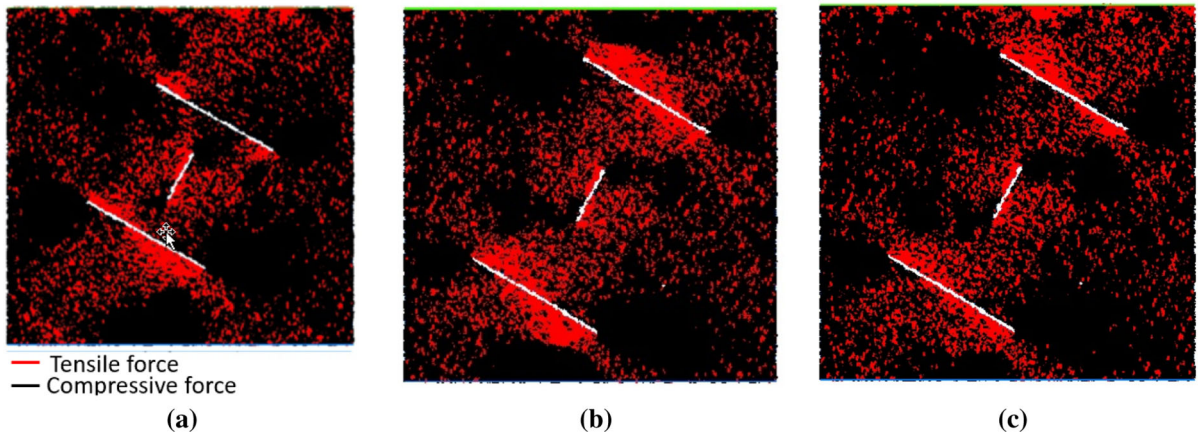


Fig. 23 Bond force distribution in models with joint spacing of **a** 2 cm, **b** 2.75 cm and **c** 3.5 cm; middle joint angle of 60°

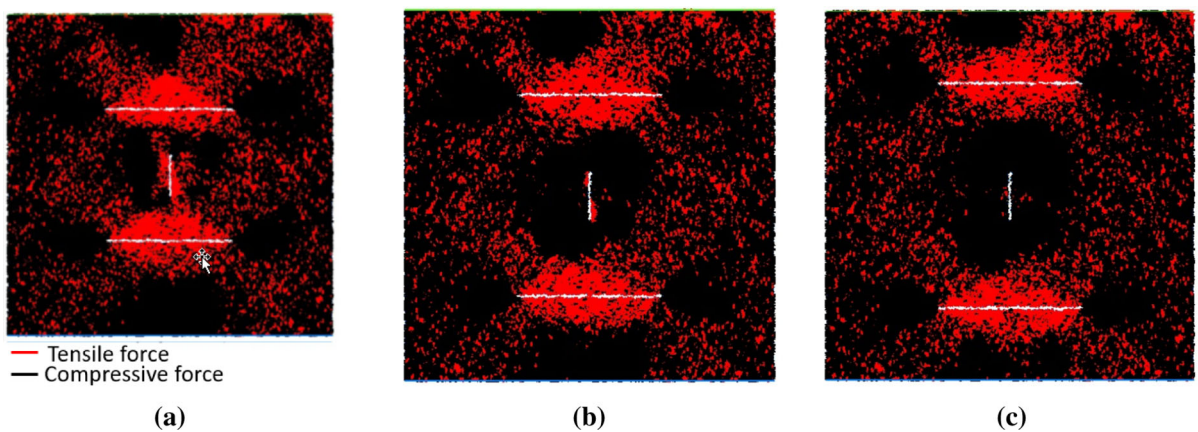


Fig. 24 Bond force distribution in models with joint spacing of **a** 2 cm, **b** 2.75 cm and **c** 3.5 cm; middle joint angle of 90°

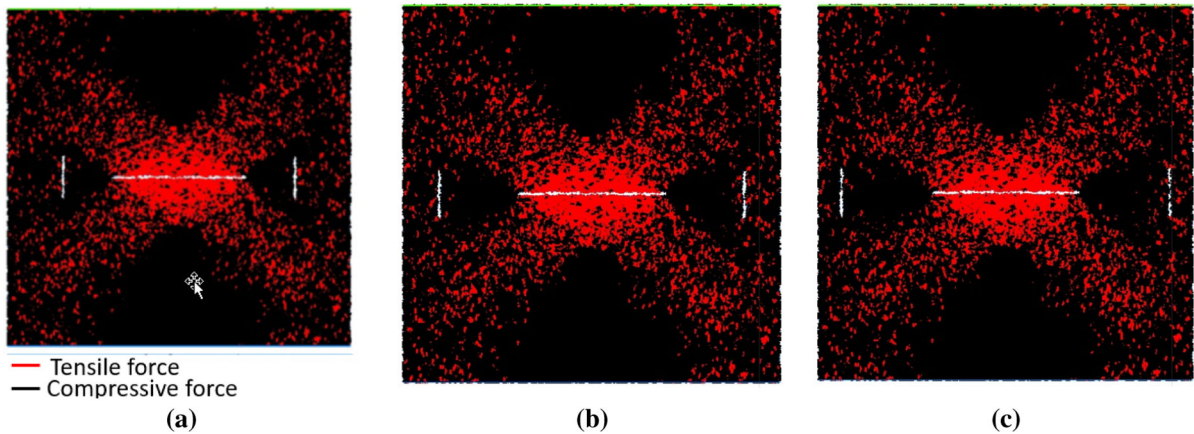


Fig. 25 Bond force distribution in models with joint spacing of **a** 2 cm, **b** 2.75 cm and **c** 3.5 cm; middle joint angle of 0°

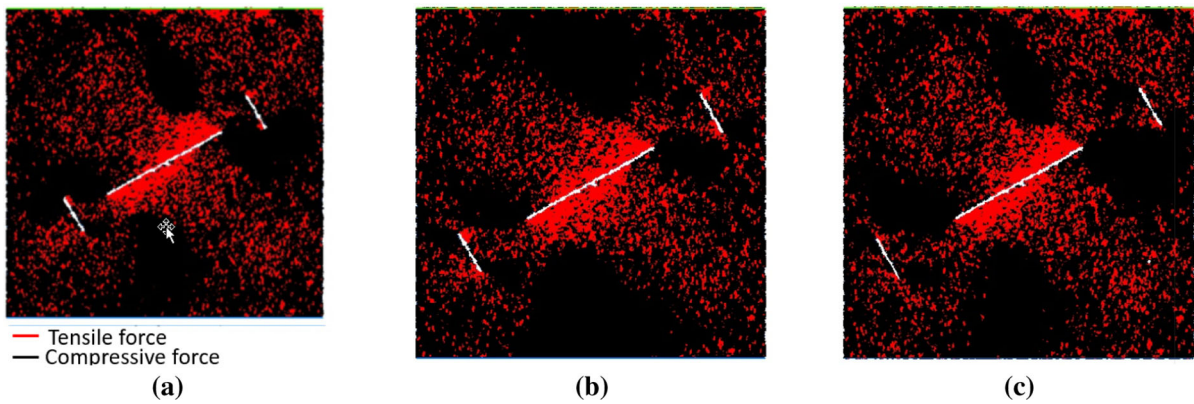


Fig. 26 Bond force distribution in models with joint spacing of **a** 2 cm, **b** 2.75 cm and **c** 3.5 cm; middle joint angle of 30°

larger joints and circulated parallel to loading axis until integrate with model boundary.

By comparison between Figs. 7–10 and Figs. 29–32, it could be concluded that the same failure patterns were occurred in experimental test and numerical simulation.

3.5.2 Small H Shape Joints

3.5.2.1 Angle of Middle Joint was 0° Figure 33 a-c indicates samples failure pattern including three non—persistent joints with middle joint angle of 0° . Red line and black line represented shear crack and tensile crack, respectively. When distance between the joints was 2, 2.75 and 3.5 cm (Fig. 33a, b and c), two tensile cracks engendered from middle joint tips and circulated parallel to loading axis until intermingle

with model boundary. Furthermore, two tensile cracks originate from middle joint wall and circulated parallel to loading axis.

3.5.2.2 Angle of Middle Joint was 30° Figure 34 a-c indicates samples failure pattern including three non—persistent joints with middle joint angle of 30° . Red line and black line represented shear crack and tensile crack, respectively. When distance between the joints was 2 cm, 2.75 cm and 3 cm (Fig. 34a, b and c), two tensile cracks engendered from middle joint tips and circulated parallel to loading axis until intermingle with model boundary. Furthermore, two tensile cracks originate from tips of larger joints and circulated parallel to loading axis until coalescence with model boundary.

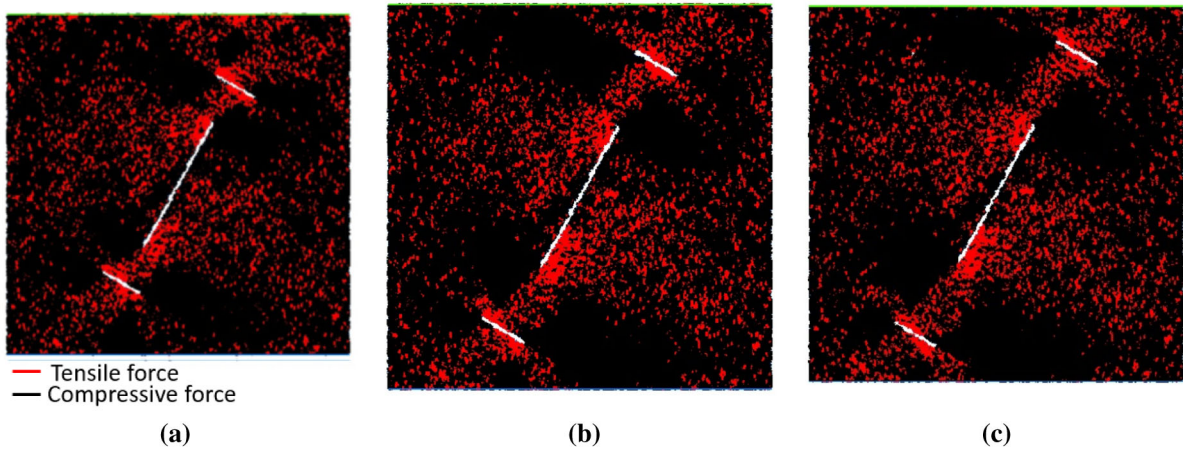


Fig. 27 Bond force distribution in models with joint spacing of **a** 2 cm, **b** 2.75 cm and **c** 3.5 cm; middle joint angle of 60°

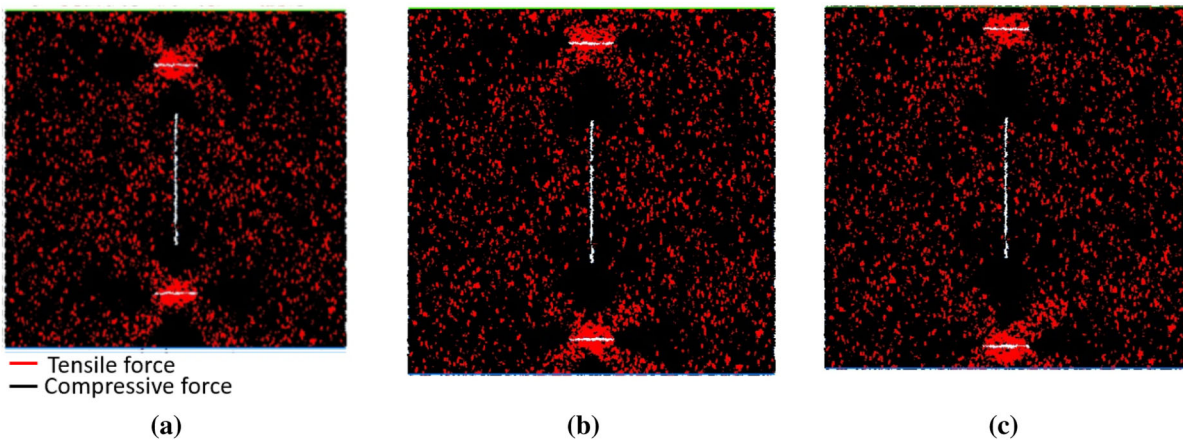


Fig. 28 Bond force distribution in models with joint spacing of **a** 2 cm, **b** 2.75 cm and **c** 3.5 cm; middle joint angle of 90°

3.5.2.3 Angle of Middle Joint was 60° Figure 35 a-c indicates samples failure pattern including three non-persistent joints with middle joint angle of 60° . Red line and black line were representative of shear crack and tensile crack, respectively. When distance between the joints was 2 cm, 2.75 cm and 3 cm (Fig. 35a, b and c), four tensile cracks originated from middle joint tips and circulated parallel to loading axis until intermingle with tips of larger joints. Furthermore, two tensile cracks originate from tips of larger joints and circulated parallel to loading axis until coalescence with model boundary.

3.5.2.4 Angle of Middle Joint was 90° Figure 36 a-c indicates samples failure pattern including three non-persistent joints with middle joint angle of

90° . Red line and black line represented shear crack and tensile crack, respectively. When distance between the joints was 2 cm, 2.75 cm and 3 cm (Fig. 36 a, b and c), several shear bands develop through the model and lead to model failure.

3.6 Ross Diagram of Crack Growth

Figure 37 shows ross diagram of crack growth for all of the notch configurations. the angles of micro cracks varied from 75 to 105 degree. it means that the variation of notch configuration have not any effect on the major fractures angle.

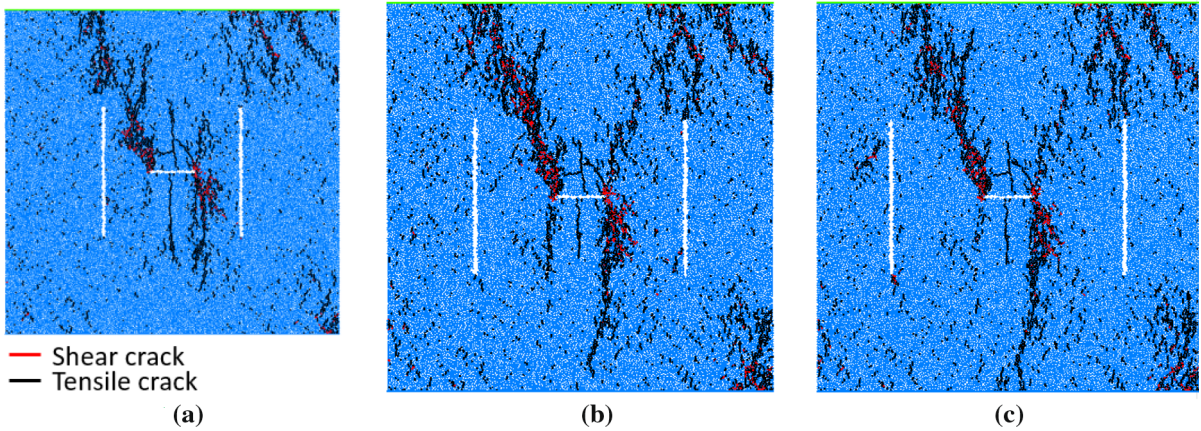


Fig. 29 Failure pattern of model containing the H shaped joints with joint spacing of **a** 2 cm, **b** 2.75 cm, **c** 3.5 m; middle joint angle of 0°

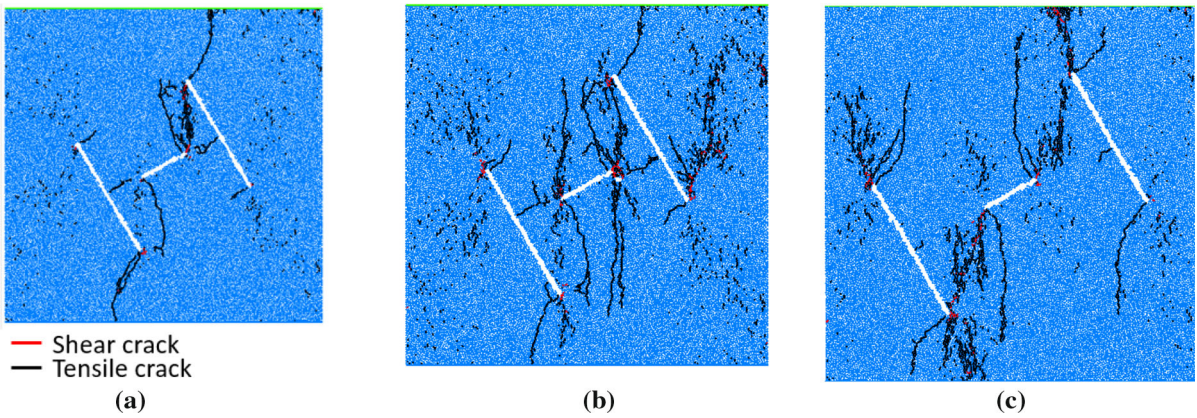


Fig. 30 Failure pattern of model containing the H shaped joints with joint spacing of **a** 2 cm, **b** 2.75 cm, **c** 3.5 m; middle joint angle of 30°

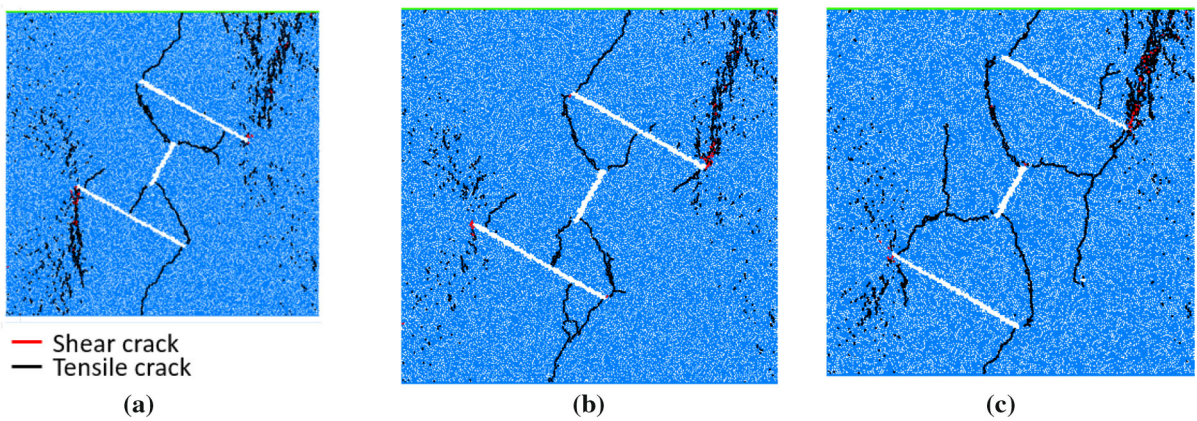


Fig. 31 Failure pattern of model including the H shaped joints with joint spacing of **a** 2 cm, **b** 2.75 cm, **c** 3.5 m; middle joint angle of 60°

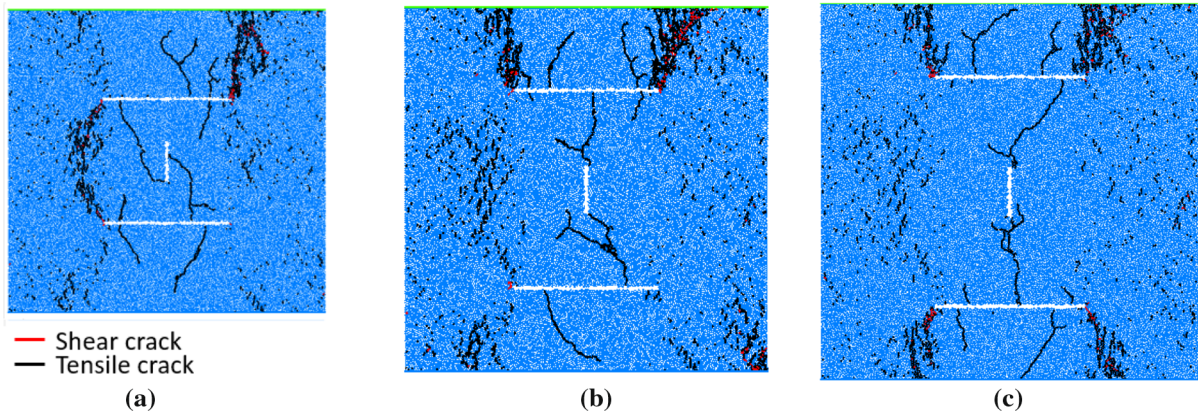


Fig. 32 Failure pattern of model containing the H shaped joints with joint spacing of **a** 2 cm, **b** 2.75 cm, **c** 3.5 m; middle joint angle of 90°

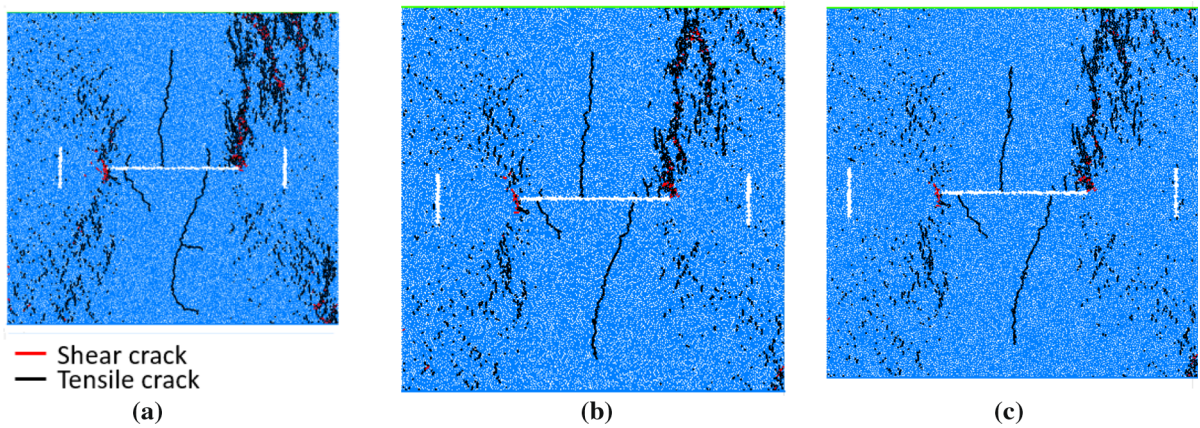


Fig. 33 Failure pattern of model containing the H shaped joints with joint spacing of **a** 2 cm, **b** 2.75 cm, **c** 3.5 m; middle joint angle of 0°

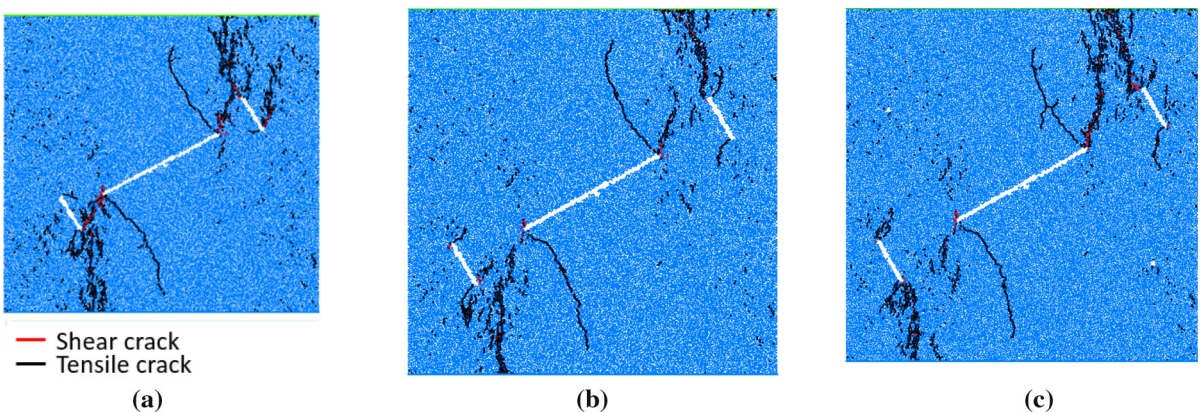


Fig. 34 Failure pattern of model containing the H shaped joints with joint spacing of **a** 2 cm, **b** 2.75 cm, **c** 3.5 m; middle joint angle of 30°

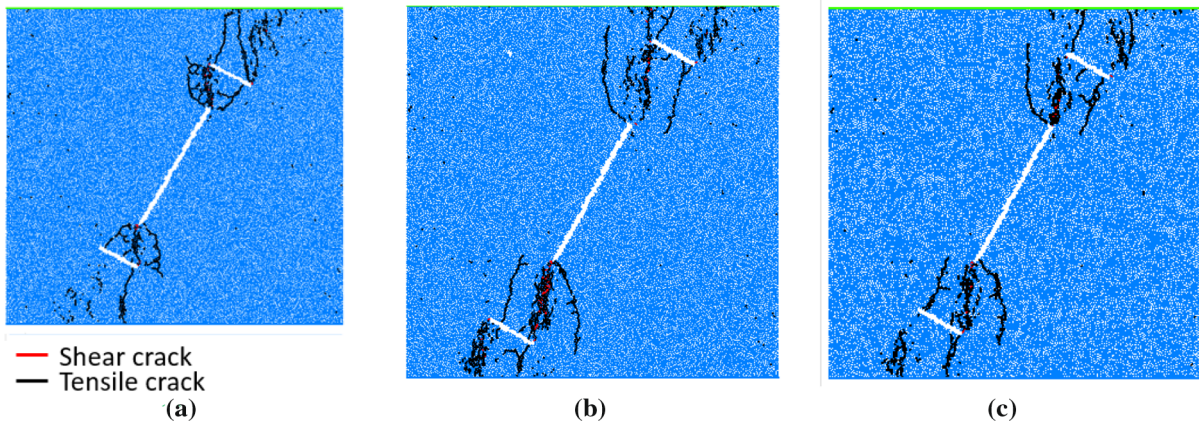


Fig. 35 Failure pattern of model containing the H shaped joints with joint spacing of **a** 2 cm, **b** 2.75 cm, **c** 3.5 m; middle joint angle of 60°

3.7 The Impact of Joint Angles on the Specimens' Strength

Figure 38 a and b represents the effects of distance between the joints on the specimens' strength for two different cases of H shape joints; i.e., large H shape joints and small H shape joints, respectively. In large H shape joints (Fig. 38a), the minimum and maximum strengths of samples occurred when joint angle were 30° and 0°, respectively. The strength of samples decreases by decreasing the distance between the joints (Fig. 38a). In this condition the stress concentration at the joints' tips increase by decreasing the distance between the joints. This leads to decreasing the compressive strength. In small H shape joints (Fig. 38b), the minimum and maximum strengths of

samples occurred when joint angle were 60° and 90°, respectively. The strength of samples decreases by decreasing the distance between the joints (Fig. 38b). In this condition the stress concentration at the joints' tips increase by decreasing the distance between the joints. This leads to decreasing the compressive strength. By comparison between Fig. 38 a and b, it could be concluded that the large joints were controlled the strength of models. In other word, when large joint has vertical configuration in large H shape joint (middle joint angle was 0°) (Fig. 38a), it has horizontal configuration in small H shape joint (middle joint angle was 90°) (Fig. 38b). In these two configurations, the model has maximum compressive strength. In constant middle joint angle, the

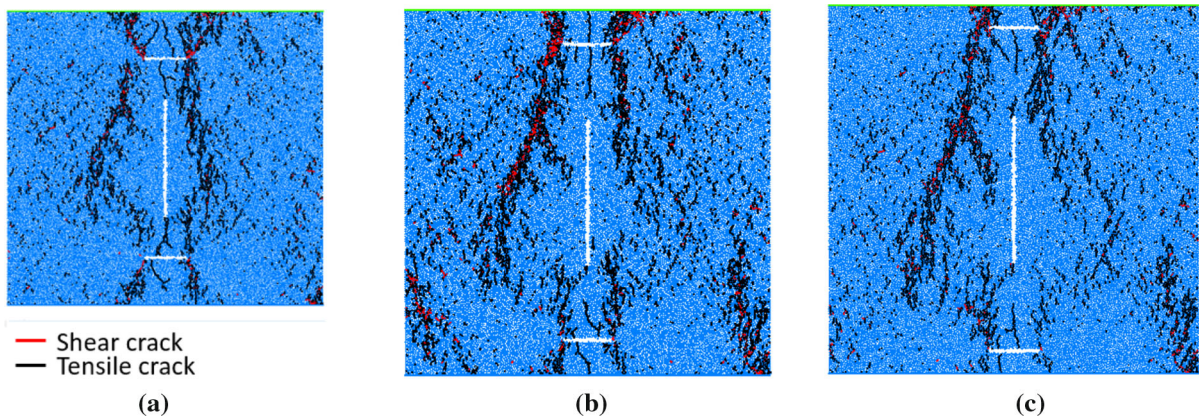


Fig. 36 Failure pattern of model containing the H shaped joints with joint spacing of **a** 2 cm, **b** 2.75 cm, **c** 3.5 m; middle joint angle of 90°

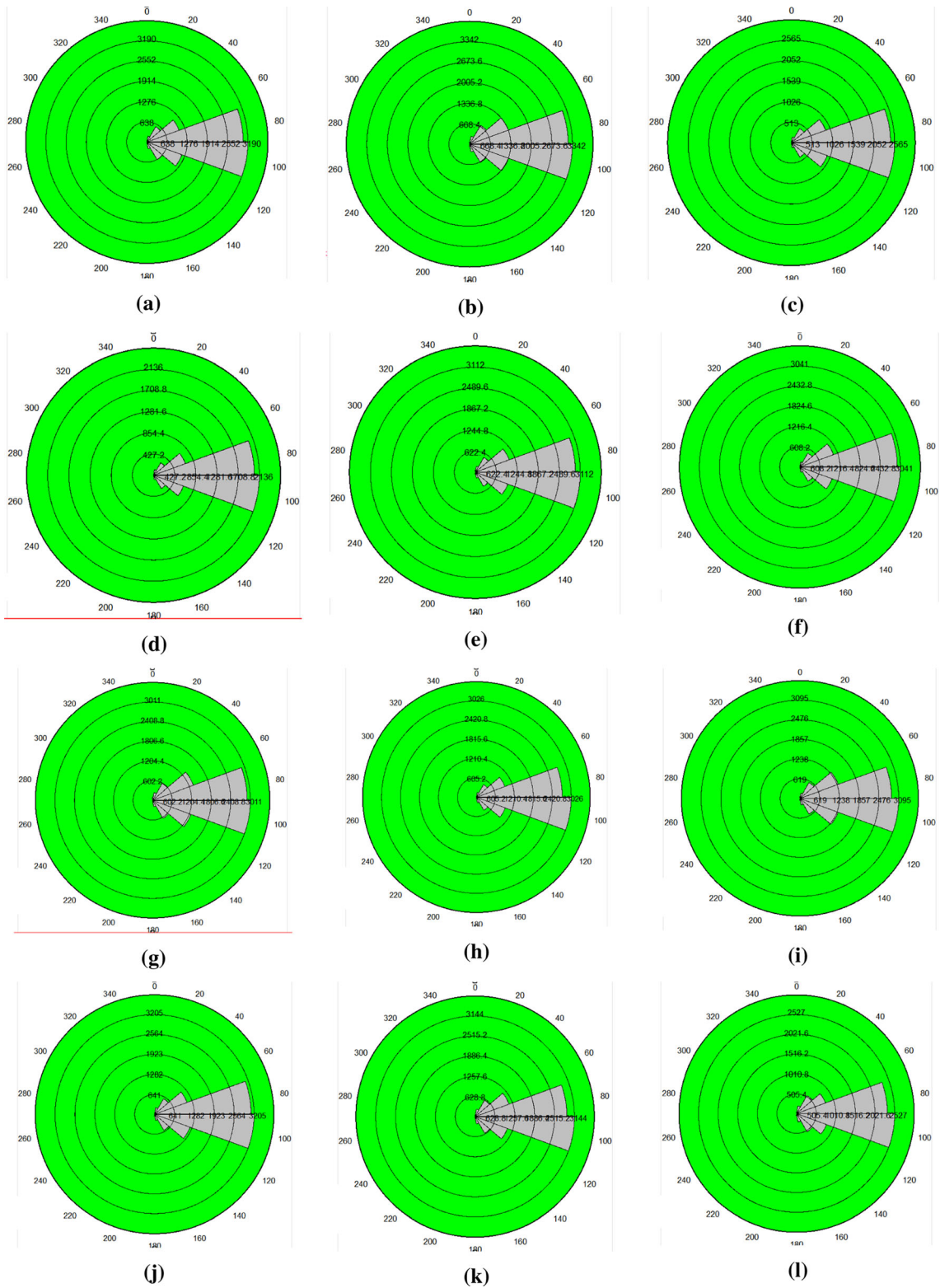


Fig. 37 Ross diagram of crack growth

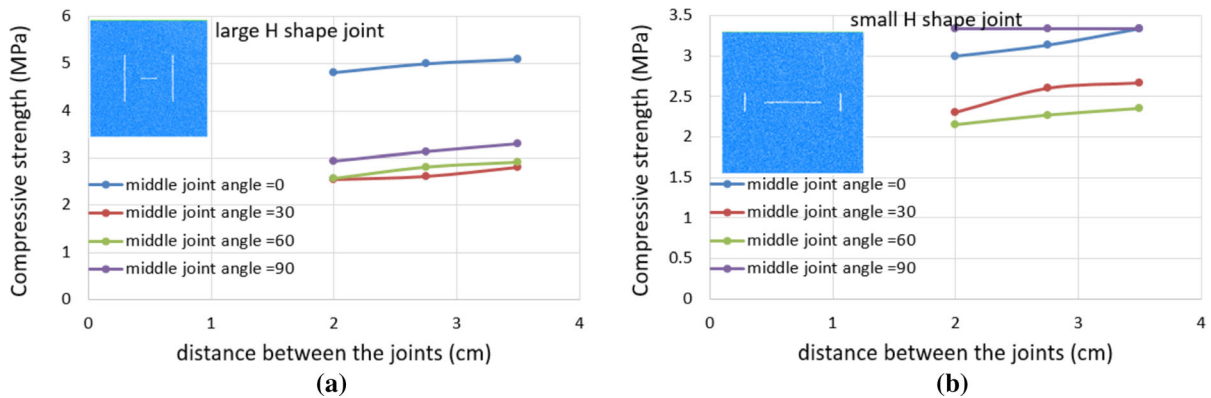


Fig. 38 Effects of distance between the joints on the specimens' strength for two different cases of H shape joints; **a** large H shape joints and **b** small H shape joints

compressive strength of models containing the large H shape joints was more than that of the small H shape joints.

By comparison between Figs. 11 and 38a, it could be concluded that the same compressive strengths were occurred in experimental test and numerical simulation.

4 Conclusion

In this paper, the failure behavior of “H” shaped non-persistent cracks under uniaxial load has been examined using experimental tests and numerical simulation. concrete with the size of 18 cm × 18 cm × 5 cm were produced. inside the sample, one “H” shaped non-persistent joints were provided. The angles of the “H” shaped non-persistent joint were 0°, 30°, 60°, and 90°. A total of 12 layouts were considered for pre-existing joints in which the larger joints were 6 cm long and the length of small crack was 2 cm. the opening of crack was 1 mm. Also, the 24 specimens with different non-persistent joints were numerically modeled. The axial load was induced to the model by a rate of 0.05 mm/min. The outcomes indicate that:

- At the tip of the crack the tensile forces of the bonded particles are greater compared to their compressive forces, therefore, the tensile crack initiation is a dominant mode of fracturing that originates at the tip of the crack within the modelled specimens. It's to be note that the tensile force was concentrated around the larger joints. It

means that the tensile cracks were originated at these locations.

- When middle joint dip was 0°, for all of the distances between the joints, two tensile cracks engendered from middle joint tips and circulated parallel to loading axis until intermingle with model boundary. Also, two tensile cracks originate from middle joint wall and circulated parallel to loading axis
- When middle joint angle was 30°, for all of the distances between the joints, two tensile cracks engendered from middle joint tips and circulated parallel to loading axis until intermingle with tips of larger joints. Also, two tensile cracks originate from tips of larger joints and circulated parallel to loading axis until coalescence with model boundary.
- When middle joint angle was 60°, for all of the distances between the joints, four tensile cracks originated from middle joint tips and circulated parallel to loading axis until intermingle with tips of larger joints. Also, two tensile cracks originate from tips of larger joints and circulated parallel to loading axis until coalescence with model boundary.
- When middle joint angle was 90°, for all of the distances between the joints, two tensile cracks originated from middle joint tips and circulated parallel to loading axis until intermingle with walls of larger joints. Also, two tensile cracks originate from walls larger joints and circulated parallel to loading axis until coalescence with model boundary.

- In large H shape joints, the minimum and maximum strengths of samples occurred when joint angle were 30° and 0° , respectively.
- In small H shape joints, the minimum and maximum strengths of samples occurred when joint angle were 60° and 90° , respectively.
- The strength of samples decreases by decreasing the distance between the joints.
- Totally the large joints angle was controlled the strength of models. In other word, when large joint has vertical configuration in large H shape joint (middle joint angle was 0°), it has horizontal configuration in small H shape joint (middle joint angle was 90°). In these two configurations, the model has maximum compressive strength. In constant middle joint angle, the compressive strength of models containing the large H shape joints was more than that of the small H shape joints.
- The same failure patterns were occurred in experimental test and numerical simulation.
- The same compressive strengths were occurred in experimental test and numerical simulation.

References

- Bahaaddini M, Sharrock G, Hebblewhite BK (2013) Numerical investigation of the effect of joint geometrical parameters on the mechanical properties of a non-persistent jointed rock mass under uniaxial compression. *Comput Geotech* 49:206–225
- Bobet A (2000) The initiation of secondary cracks in compression. *Eng Fract Mech* 66:187–219
- Brideau MA, Yan M, Stead D (2009) The role of tectonic damage and brittle rock fracture in the development of large rock slope failures. *Geomorphology* 103:30–49
- Chen M, Yang SQ, Ranjith PG (2019a) Fracture processes of rock-like specimens containing non persistent fissures under uniaxial compression. *Energies* 12(1):71–81
- Chen SJ, Yin DW, Jiang N (2019b) Mechanical properties of oil shale-coal composite samples. *Int J Rock Mech Min* 123:99–111
- Cheng Y, Wong LNY (2018) Microscopic characterization of tensile and shear fracturing in progressive failure in marble. *J Geophys Res Solid Earth* 123:204–225
- DeSilva VRS, Ranjith PG, Wu BS, Perera MSA (2018a) Micro-mechanics based numerical simulation of nacl brine induced mechanical strength deterioration of sedimentary host-rock formations. *Eng Geol* 242:55–69
- DeSilva VRS, Ranjith PG, Perera MSA (2018b) A low energy rock fragmentation technique for in-situ leaching. *J Clean Prod* 204:586–606
- Einstein HH, Veneziano D, Baecher GB, O'Reilly KJ (1983) The effect of discontinuity persistence on rock slope stability. *Int J Rock Mech Min Sci Geomech Abs* 20(5):227–236
- Esterhuizen GS, Dolinar DR, Ellenberger JL (2011) Pillar strength in underground stone mines in the United States. *Int J Rock Mech Min* 48(42):50
- Farahmand K, Vazaios I, Diederichs MS, Vlachopoulos N (2018) Investigating the scale dependency of the geometrical and mechanical properties of a moderately jointed rock using a synthetic rock mass (SRM) approach. *Comput Geotech* 95:121–132
- Fu JW, Chen K, Zhu WS, Zhang XZ, Li XJ (2016) Progressive failure of new modelling material with a single internal crack under biaxial compression and the 3-D numerical simulation. *Eng Fract Mech* 165:140–152
- Ghazvinian A, Sarfarazi V, Schubert W, Blumel M (2012) A study of the failure mechanism of planar non-persistent open joints using PFC2D. *Rock Mech Rock Eng* 45(5):677–693
- Huang D, Cen DF, Ma GW, Huang RQ (2015) Step-path failure of rock slopes with intermittent joints. *Land Slides* 12(5):911–926
- Huang YH, Yang SQ, Tian WL (2019) Crack coalescence behavior of sand stone specimen containing two pre-existing flaws under different confining pressures. *Theor Appl Fract Mec* 99:118–130
- Jiang Y, Luan H, Wang D (2020) Failure mechanism and acoustic emission characteristics of rock specimen with edge crack under uniaxial compression. *Geotech Geol Eng* 37:2135–2145
- Lajtai EZ (1974) Brittle fracture in compression. *Int J Fracture* 10:525–536
- Lajtai EZ, Carter BJ, Duncan EJS (1994) Enechel on crack-arrays in potash salt rock. *Rock Mech Rock Eng* 27:89–111
- Lee H, Joo S (2011) An experimental and numerical study of fracture coalescence in precracked specimens under uniaxial compression. *Int J Solids Struct* 48:979–999
- Lei XL, Masuda K, Nishizawa O (2004) Detailed analysis of acoustic emission activity during catastrophic fracture of faults in rock. *J Struct Geol* 26:247–258
- Li DY, Zhu QQ, Zhou ZL (2017) Fracture analysis of marble specimens with a hole under uniaxial compression by digital image correlation. *Eng Fract Mech* 183:109–124
- Naderloo M, Moosavi M, Ahmadi M (2019) Using acoustic emission technique to monitor damage progress around joints in brittle materials. *Theor Appl Fract Mec* 104:67–81
- Park CH, Bobet A (2010) Crack initiation, propagation and coalescence from frictional flaws in uniaxial compression. *Eng Fract Mech* 77:2727–2748
- Pine RJ, Owen DRJ, Coggan JS, Rance JM (2007) A new discrete fracture modelling approach for rock masses. *Geotechnique* 57(9):65–78
- Potyondy DO (2012) A flat-jointed bonded-particle material for hard rock. *US Rock Mechanics/Geomechanics Symposium*
- Potyondy DO (2015) The bonded-particle model as a tool for rock mechanics research and application: Current trends and future directions. *Geosyst. Eng* 18(1):1–28

- Potyondy DO (2017) Simulating perforation damage with a flat-jointed bonded-particle material. US Rock Mechanics/ Geomechanics Symposium
- Potyondy DO, Cundall PA (2004) A bonded-particle model for rock. *Int J Rock Mech Min Sci* 41:1329–1364
- Prudencio M, VanSintJan M (2007) Strength and failure modes of rock mass models with non-persistent joints. *Int J Rock Mech Min* 44:890–902
- Sagong M, Bobet A (2002) Coalescence of multiple flaws in a rock-model material in uniaxial compression. *Int J Rock Mech Min* 39:229–241
- Shi G.H (1992) Modeling rock joints and blocks by manifold method, The 33 th US Symposium on Rock Mechanics, American Rock Mechanics Association.
- Siad L, Megueddem M (1998) Stability analysis of jointed rock slope. *Mech Res Commun* 25(6):661–670
- Song Y (2020) Experimental and numerical study on crack-arrest behaviours of rock-like SCDC specimens. *Geotech Geol Eng* 38:6795–6807
- Sun XZ, Li JZ (2019) Numerical study on crack propagation characteristics under different loading conditions by FRACOD2D approach. *Geotech Geol Eng* 37:91–69
- Sun XZ, Wang HL, Liu KM, Zhan XC (2020) Experimental and numerical study on mixed crack propagation characteristics in rock-like material under uniaxial loading. *Geotech Geol Eng* 38:191–199
- Wang J (2019) Numerical analysis of crack propagation evolution of specimens with different dip angles of cross fractures. *Geotech Geol Eng* 37:2535–2544
- Wang SY, Sloan SW, Sheng DC, Yang SQ, Tang CA (2014) Numerical study of failure behavior of pre-cracked rock specimens under conventional triaxial compression. *Int J Solids Struct* 51:1132–1148
- Wang YT, Zhou XP, Wang Y, Shou YD (2018) A 3-Dconjugatedbond-pair-based peridynamic formulation for initiation and propagation of cracks in brittle solids. *Int J Solids Struct* 134:89–115
- Wang J, Ning JG, Qiu PQ, Yang S, Shang HF (2019) Microseismic monitoring and its precursory parameter of hard roof collapse in long wall faces: a case study. *Geomech Eng* 17(4):375–383
- Wong LNY, Einstein HH (2009) Crack coalescence in molded gypsum and carrara marble: part2—microscopic observations and interpretation. *Rock Mech Rock Eng* 42:513–545
- Wong R, Chau K, Tang C, Lin P (2001) Analysis of crack coalescence in rock-like materials containing three flaws—partI: experimental approach. *Int J Rockmech Min* 38:909–924
- Wu X (2020) Crack initiation and failure mechanism of granite with single crack. *Geotech Geol Eng* 38:651–661
- Wu TH, Gao YT, Zhou Y, Li JW (2020) Experimental and numerical study on the interaction between holes and fissures in rock-like materials under uniaxial compression. *Theor Appl Fract Mech* 106:54–67
- Yang XX, Kulatilake PHSW, Jing HW, Yang SQ (2015) Numerical simulation of a jointed rock block mechanical behavior adjacent to an underground excavation and comparison with physical model test results. *Tunn Undergr Sp Tech* 50:129–142
- Yang H, Liu J, Wong LNY (2017) influence of petroleum on the failure pattern of saturated pre-cracked and intact sandstone. *B Eng Geol Environ* 77:767–774
- Yang WD, Li GZ, Ranjith PG, Fang LD (2019) An experimental study of mechanical behavior of brittle rock-like specimens with multi-non-persistent joints under uniaxial compression and damage analysis. *Int J Damage Mech* 28(10):1490–1522
- Zang CW, Chen M, Zhang GC, Wang K (2020) Research on the failure process and stability control technology in a deep roadway: numerical simulation and field test. *Energy Sci Eng* 12(2):33–44
- Zhang H, Wang LNY (2012) Cracking processes in rock-like material containing a single flaw under uniaxial compression: a numerical study based on parallel bonded-particle model approach. *Rock Mech Rock Eng* 45:711–737
- Zhang GL, Ranjith PG, Wu BS (2019) Synchrotron X ray tomographic characterization of microstructural evolution in coal due to supercritical CO₂ injection at in-situ conditions. *Fuel* 255:33–42
- Zhou XP, Zhang YX, Ha QL (2008) Real-time computerized tomography (CT) experiments on limestone damage evolution during unloading. *Theor Appl Fract Mec* 50(1):49–56
- Zhou XP, Cheng H, Feng YF (2014) An experimental study of crack coalescence behavior in rock-like materials containing multiple flaws under uniaxial compression. *Rock Mech Rockeng* 47(6):1961–1986

Publisher's Note Springer Nature remains neutral with regard to jurisdictional claims in published maps and institutional affiliations.